

19 High Resolution Imaging in the Graphene Liquid Cell

Jungwon Park, Vivekananda P. Adiga, Alex Zettl, and A. Paul Alivisatos

19.1 Introduction to Graphene Liquid Cells: Advantages, Opportunities, and Fabrication Methods

Developments in electron microscopy of liquids provide visual insights into structure and function in physical and biological chemistry. The ultimate goal of liquid microscopy is to see materials in action with the greatest possible detail. Atomic resolution offers significant advantages in understanding phenomena associated with biological materials, electrochemical reactions, or nanoparticle growth in liquid environments. Conventional electron microscopy offers superb resolution. In liquid environments, atomic resolution initially eluded scientists and microscopists, even though diverse applications of the initial liquid cell design, based on silicon nitride, confirmed that liquid cell microscopy has the potential to achieve nanoscale resolution. The more recent development of the graphene liquid cell (GLC) now provides the chance to improve liquid cell resolution by using an atomically thin inert material, graphene, as the window material [1–6]. In this chapter, we outline the development of the GLC and its use in studying colloidal nanoparticles, bio-inorganic conjugated nanostructures, and protein molecules.

Graphene has emerged as a versatile membrane material for all types of TEM experiments [2, 7, 8] due to its electron transparency and favorable electrical, mechanical, and thermal properties. The strong van der Waals interaction between graphene sheets, together with graphene's impermeability to liquids and gases, makes it an ideal material to enable the trapping of small pockets of liquid containing a material of interest for TEM imaging [1]. The first generation design of GLCs can be used in a conventional TEM without modification or customization of either the TEM or the holder. The most elementary geometry, and that employed in the original GLC experiments [1], consists of two sheets of monolayer graphene arranged in a bubble-wrap or blister-like configuration, as illustrated in Figure 19.1. These GLCs were produced by transferring graphene grown by chemical vapor deposition (CVD) onto commercially available TEM grids by a direct transfer method [9], in which two gold TEM grids covered with a holey carbon film with well-defined periodic perforations (also known as Quantifoil®) are placed on CVD-grown graphene on copper, then the copper is removed using wet etching. The graphene on the grid is then transferred through several de-ionized water baths. After placing a drop of the solution of interest on one of the

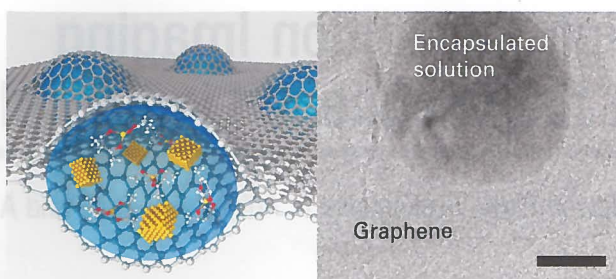


Figure 19.1. Conceptual diagram of the first generation GLC, where van der Waals interaction between two graphene sheets is used to trap the liquid, and a TEM image of the trapped liquid. The scale bar is 50 nm. Reproduced from Ref. 1 with permission from AAAS.

grids, the second grid is placed on top to create a sandwich structure where liquid is trapped in multiple blisters between the two graphene layers. Such blisters show circular shapes with a wide size range. Their diameter and thickness, as measured by atomic force microscopy, are tens of nanometers to micrometers. Blisters at the smaller end of the size range, typically <100 nm in diameter, have been used for atomic resolution imaging of liquid-borne metal nanocrystals [1], without the scattering and undesirable charging effects endemic to silicon nitride-based liquid cells.

The graphene has several key advantages when used in this way. The chemical and physical inertness of its surface helps in trapping biological samples without them being non-specifically adsorbed onto the blister walls. Unlike the artificial adhesion from the spacers in microfabricated liquid cells [10–21], the strong van der Waals attraction between the two graphene layers of the GLC minimizes contamination and leakage during sample preparation and observation. More importantly, for imaging delicate samples in liquid, the high electrical and thermal conductivities of graphene enable fast transfer of accumulated charges or heat due to the electron beam, and it is therefore a promising system to minimize radiation damage. Despite these advantages, controlling the size and shape (including aspect ratio) of the liquid chamber in these simple GLCs has been challenging. This difficulty is partly due to graphene's low bending rigidity, which often leads to irreversible collapse of the sheets onto each other giving a random overall thickness of the entrapped liquid packet. Similarly, the generation of bubbles by radiolysis (Chapter 7) can dynamically alter the overall size of the liquid packet in unpredictable ways. These limitations have led to the development of second generation GLCs.

Second generation GLCs (H. I. Rasool, private communication) are shown in Figure 19.2. They are made by transferring graphene onto highly regular prefabricated through-holes in thin (<200 nm) silicon nitride membranes. Strong adhesion between graphene and Si_xN_y results in size-controlled liquid packets trapped between the graphene sheets separated by the perforated Si_xN_y spacer. Perforated membranes are commercially available or can be fabricated with conventional photolithographic or focused ion beam techniques. Typical through-holes in Si_xN_y are in the size range of 100 nm to 1 μm . The perforated membranes can be pretreated with oxygen plasma

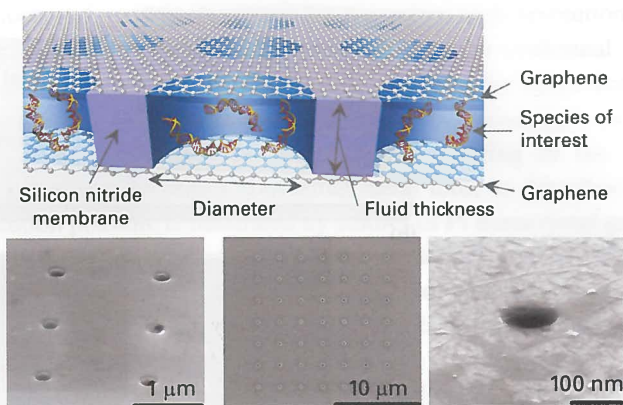


Figure 19.2. Schematic of liquid-filled, graphene-encapsulated perforations in a Si₃N₄ membrane, and SEM images of graphene-covered perforations in Si₃N₄ filled with liquid. Images courtesy Haider I. Rasool.

to make them hydrophilic. In one construction method, thin PMMA (20 nm) is spin-coated onto CVD-grown graphene/copper followed by wet etching of the copper in ammonium persulfate solution. The PMMA/graphene film is rinsed with deionized water, then transferred onto the wafer side of a perforated Si₃N₄ membrane on a Si wafer. Finally, another graphene/PMMA film is floated in a solution of the liquid of interest, then transferred to the top surface of the Si₃N₄/graphene/PMMA substrate. To ensure sealing, drying must be done following the transfer. Finally, the PMMA film is removed using acetone/IPA. The result is a trapped liquid packet of pre-defined volume. However, this method also has its challenges. It is difficult to trap liquid/buffer solutions in small holes (<500 nm), but in large holes (1 μm or larger) the graphene sheets from both sides tend to collapse onto each other, resulting in problems similar to those discussed for the first generation design. Bubble formation from radiolysis can result in variations in pH [22, 23] and variable liquid thickness inside the cell, complicating the analysis of the data.

Some of these problems can be resolved by third-generation GLCs, called graphene liquid flow cells (GLFCs) because they employ controlled liquid flow (Figure 19.3) [24]. Liquid cells with flow capabilities have advantages when studying chemical reactions that require initiation on demand or continuous refreshing of the liquid environment. Using flow in microfabricated liquid cells with Si₃N₄ windows can be difficult: the windows deform or bow under the pressure difference between flowing liquid and vacuum, creating liquid layers that are too thick for many kinds of nanoscale imaging [24]; the flow can be non-uniform; and bubble formation [22] also may cause unstable flow due to the membrane flexibility. The third-generation GLC adopts the beneficial aspects of flow established in Si₃N₄-based cells, but uses graphene technology to bypass some of the limitations.

The third-generation GLFC is not simply a conventional flow cell design with graphene replacing the Si₃N₄. The poor bending stiffness of graphene and difficulty in

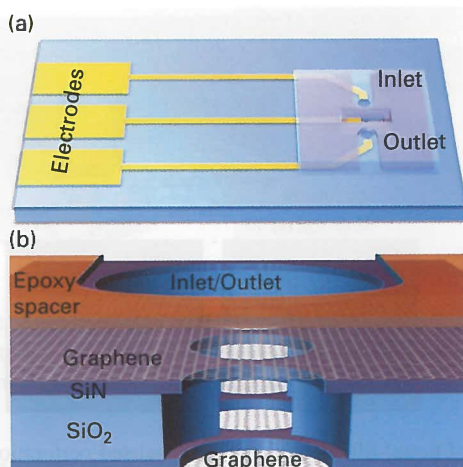


Figure 19.3. Conceptual design of a fully integrated nanofluidic channel that can be accommodated in existing electrochemical TEM holders. Two electrodes enable liquid flow through a nanofluidic channel formed by Si_xN_y membranes. The electrodes aid the motion of particles and molecules under the influence of an electric field using electrophoretic means. Also shown is a cross-sectional view of the flow cell with openings in the Si_xN_y window covered with graphene. From Ref. 24.

obtaining intact graphene sheets over large areas without pinholes makes it difficult to directly replace the Si_xN_y windows with graphene for flow cells. Instead, as shown in Figure 19.3, the flow region is a nanofluidic channel (1 μm wide) etched in a silicon dioxide layer (100 nm thick) sandwiched between thin (e.g. about 50 nm thick) Si_xN_y layers. These Si_xN_y layers have well-defined perforations (e.g. having dimensions of about 100 nm) sealed by few-layer graphene that serves as viewports for electron imaging. The small hole size in the Si_xN_y results in limited bowing of the graphene and hence controls the overall liquid thickness better. The channel in such a flow cell is capable of sustained liquid flow and can be electrically contacted for aiding the movement of particles in the liquid. These hybrid nanofluidic channels are expected to improve functionality and overall reliable resolution significantly.

19.2 Studying Growth Mechanisms in Atomic Detail by GLC-TEM

The first-generation GLC has enabled imaging of both growth and diffusion of nano-scale crystals. Below we highlight some of these results, illustrating the types of phenomena and data that are accessible through GLC experiments.

19.2.1 Nanocrystal Growth at Atomic Resolution

Transparency to the imaging electrons (which reduces background in the images) and surface inertness (which reduces crystal–wall interactions) enable us to study atomistic

details of nanocrystal growth dynamics by recording high resolution *in situ* TEM movies in the GLC. Assuming that the graphene forms a conformal wrap over the encapsulated growth solution, we explore the sample at low magnification to search for liquid pockets whose diameter is <100 nm. This minimizes excessive liquid thickness and hence unwanted scattering. During imaging of the liquid packet, nanoparticles grow from solutions containing metal ions, as described in Chapter 9. The high resolution possible is illustrated by studies of Pt nanocrystal growth in GLCs obtained using aberration-corrected TEM [1]. Spherical and chromatic aberration correction contribute to the exceptionally high resolution and enhanced signal-to-noise ratio while the graphene membrane remains intact over the entire time period of observation.

Previous *in situ* studies by other types of liquid cell TEM and X-ray scattering have shown that nanocrystals in solution grow both by monomer addition and by frequent coalescence events [1, 19, 26–28]. The GLC allows direct observation of critically important features of the coalescence process at a higher resolution. Figure 19.4 shows

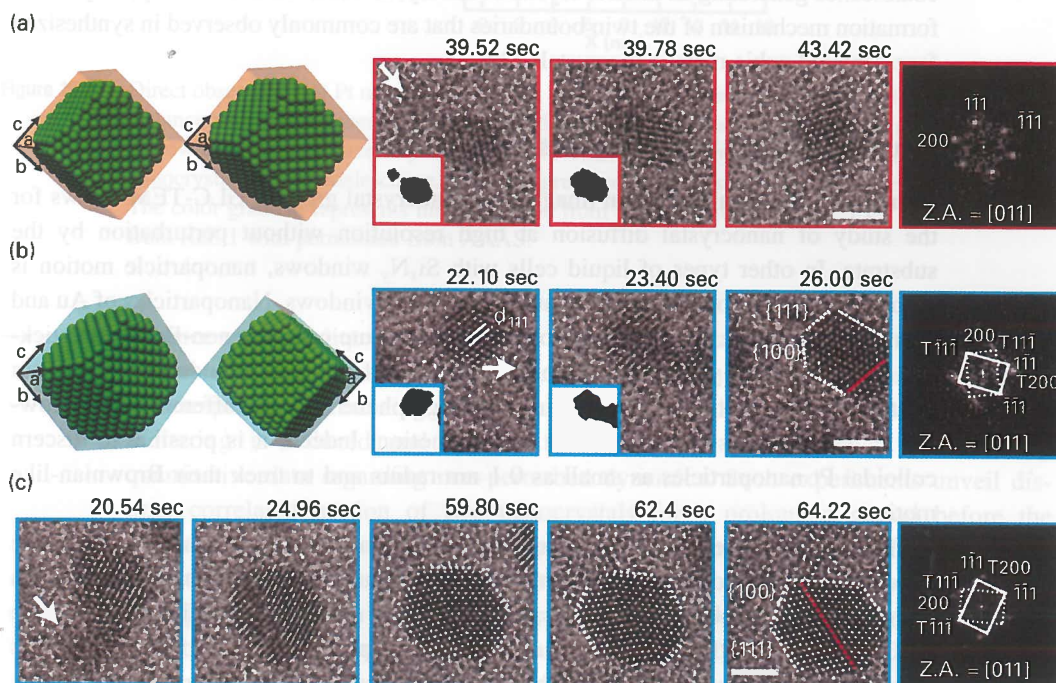


Figure 19.4. Atomic resolution image series obtained during Pt nanocrystal growth in a GLC in TEM. The images exhibit preferential coalescence along $\langle 111 \rangle$ directions which evolves into (a) a single crystalline face-centered cubic structure or (b) a twinned face-centered cubic structure. Incoming small nanocrystals are marked with white arrows. Black and white insets represent thresholded volume projections that clarify the nanocrystal shapes and positions. (c) Image series obtained during Pt nanocrystal shape evolution shows the straightening of the twin boundary and evolution towards a hexagonal shape consistent with the Wulff construction. FFT images for (a)–(c) correspond to the final frame of each sequence. Scale bars are 2 nm and zone axis is abbreviated as Z.A. Reproduced from Ref. 1 with permission from AAAS.

the beam-induced formation of Pt nanocrystals and subsequent crystal growth by coalescence. The crystallographic orientation relationship of the joining nanocrystals can be seen [1]. The most interesting finding is that most coalescence events proceed along one particular nanocrystal orientation, $\{111\}$. Once nanocrystals collide at $\{111\}$ planes, they merge quickly, within the acquisition speed of one frame (0.26 s). Exposed $\{111\}$ surfaces of a face-centered cubic crystal are known to have the lowest surface energy, therefore perhaps the lowest ligand coverage; incoming particles may thus experience minimal ligand obstruction. In this scenario, nanocrystals that contact at $\{111\}$ planes quickly unify to minimize the total surface area and thus energy [29]. Contact that joins identically oriented crystals is shown in Figure 19.4a. Alternatively, contact that joins mirror $\{111\}$ planes (Figure 19.4b and c) yields nanocrystals with a twin boundary. In addition, structural rearrangements of the nanoparticles are visible. These occur mainly by surface diffusion and rearrangement. Surface diffusion evolves the nanocrystal shape after coalescence from quasi-spherical to a hexagonal shape that minimizes surface energy, as expected from a Wulff construction (Figure 19.4c). Particle coalescence generating an interior crystal boundary, as observed in this study, may be the formation mechanism of the twin boundaries that are commonly observed in synthesized face-centered cubic metal nanocrystals [29].

19.2.2 Diffusion Dynamics of Nanocrystals

Along with the high resolution imaging of nanocrystal growth, GLC-TEM allows for the study of nanocrystal diffusion at high resolution without perturbation by the substrate. In other types of liquid cells with Si_xN_y windows, nanoparticle motion is perturbed by the strong potential of attraction to the windows. Nanoparticles of Au and Pt in non-graphene cells have been observed to execute complex non-Brownian stick-slip motion, possibly due to weak binding to one of the Si_xN_y windows [11, 19]. In contrast, the interaction of nanoparticles with graphene appears different, since growing Pt nanoparticles do not show stick-slip motion. Indeed, it is possible to discern colloidal Pt nanoparticles as small as 0.1 nm radius and to track their Brownian-like motion.

The motions observed in GLC experiments are much slower than what would be expected in an unconfined fluid with the normal bulk viscosity. Slow diffusion, in both Si_xN_y and graphene liquid cells, is discussed in more detail in Chapter 13. In the GLC, it is possible that sub-100 nm diameter liquid pockets may confine the particles significantly. But equally, it is possible that a few layers of solvent organic molecules near the substrate might retard particle dynamics locally. It may in fact be the case that particles in the center of any liquid cell are moving too quickly to be observed at the TEM frame rate, and only those particles that are confined between graphene windows in small liquid pockets move slowly enough to be tracked. The absence of stick-slip motion perhaps suggests a general slowing of diffusion, rather than surface interactions at particular locations. Thus it is probably the case that growth trajectories observed in GLCs may reveal events that can be hidden or distorted in the growth trajectories in non-graphene liquid cells.

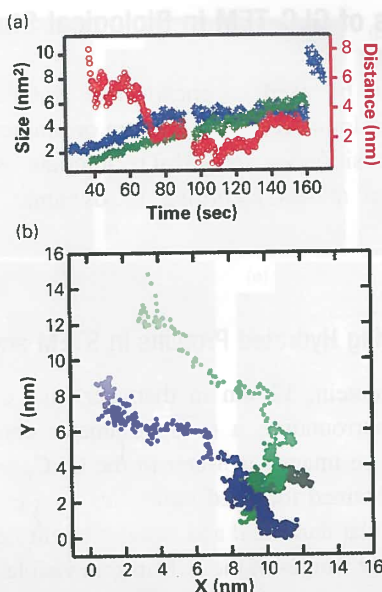


Figure 19.5. Direct observation of Pt nanocrystal growth and diffusion dynamics in the GLC. (a) The projected distance between two nanocrystals (red) and the projected sizes (blue and green) measured during a growth and coalescence sequence. (b) Two-dimensional projected position change of the two nanocrystals before coalescence. Blue and green colors correspond to the nanocrystals in (a). The color gradient represents time evolution from 40 s (bright) to 160 s (dark). Reproduced from Ref. 1 with permission from AAAS.

Since multiple liquid pockets with different sizes are formed in a GLC, a liquid pocket with optimal size can be selected for imaging, depending on the scale of the sample. By minimizing the extra amount of liquid over the sample, background scattering is reduced and contrast increased. This is important for obtaining quantitative data regarding non-perturbed dynamics. Such experiments unveil distinct correlated motion of two nanocrystals for a prolonged period before the particles join along the $\{111\}$ orientation. In Figure 19.5a, b, blue and green trajectories show particle size, center-to-center distance, and position change during a coalescence event. Initially the freely moving nanocrystals draw close and the center-to-center distance rapidly decreases. This is followed by fluctuation of the center-to-center separation (here, between 1 and 6 nm) for the next 25 s. While this dynamic event proceeds, the nanocrystals also grow in size gradually by monomer addition. The sustained correlated motion in a confined regime exhibits three-dimensional behavior, collision, rolling, and relative sliding of nanocrystals over each other. Knowing the surface ligand length of 1 to 2 nm, these motions occur while the surface ligand layers touch and interleave [30]. After a prolonged period of this correlated motion, the center-to-center distance approaches the sum of the radii of the two nanocrystals and the nanocrystal lattices align, leading to coalescence.

19.3 Applications of GLC-TEM in Biological Studies

The GLC can be used to encapsulate water that contains biological materials. This allows exploration of the structure of biomolecules in the hydrated state, including their composition via analytical techniques, as well as evaluation of electron beam effects. It also allows recording of dynamic processes as biomolecules diffuse in water.

19.3.1 GLC for Studying Hydrated Proteins in STEM and EELS

Ferritin is a protein, 12 nm in diameter, that consists of a spherical protein shell (apo-ferritin) surrounding a 6 nm diameter core of hydrous ferric oxide. Ferritin molecules can be imaged in water in the GLC, and the results can then be compared with images obtained for dried molecules on a graphene substrate. Figure 19.6 shows high angle annular dark field and annular bright field STEM images of ferritin within a GLC, with lattice fringes of the ferritin core visible (Figure 19.6c). The resolution in this experiment even enables individual Fe atoms in water to be distinguished at the edge of the GLC (Figure 19.6d, e).

A key result of such studies is that beam-induced damage at 80 kV appears to be significantly reduced in the presence of liquid [3]. Furthermore, mass loss during EELS measurement is reduced if the sample is encapsulated by graphene [3]. In Figure 19.7, Fe from the cores and N and O from the protein shell are clearly resolved in EELS mapping of graphene-protected samples, whereas unprotected samples show significant mass loss of oxygen and nitrogen. The GLC-TEM appears to promise the potential of quantifying the charge state of Fe in the core in the presence of water via EELS fine structure (Figure 19.7c, d).

To minimize beam damage in these measurements, dose rate (rather than dose) appears to be critical in STEM imaging, if bubble formation is used as an indicator of beam-induced physical and chemical changes of the system [22]. It is therefore possible to define conditions for successful imaging of biological samples in STEM mode that minimize electron beam damage, by keeping the dose rate below a critical limit and decreasing the pixel dwell time. Presumably, below the threshold dose rate, the energy deposited by the incoming electrons can be dissipated in the GLC by the high thermal and electrical conductance of graphene and liquid [3].

Although the GLC therefore appears to be beneficial in imaging delicate biological samples, the question still remains how the environment in the GLC stabilizes the chemical bonding and assembly of macromolecules during irradiation. Direct structural observation of macromolecules in the GLC and comparison with structures obtained from methods such as cryo-EM and X-ray crystallography is needed to address this question quantitatively. The protection of the sample against mass loss by graphene hints at exciting future possibilities for the GLC in EELS measurements.

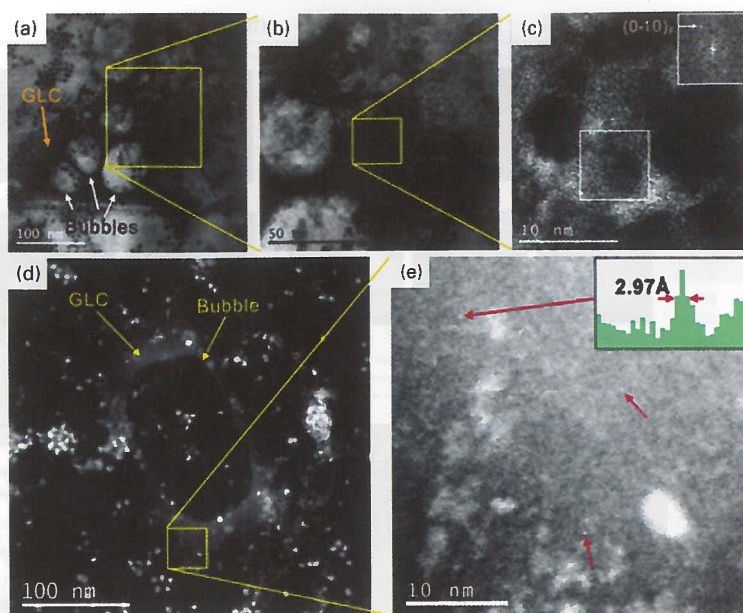


Figure 19.6. Annular bright field (a, b, c) and high angle annular dark field (d, e) STEM images of ferritin imaged in GLC TEM. Bubbles in (a), (b), and (d) were formed in advance using the Ronchigram mode to confirm the presence of liquid. Then, in STEM mode, electron dose rate and pixel dwell time were optimized to form no further bubbles during scanning. An inset in (c) shows FFT patterns of an area containing ferritin to confirm lattice spacing of the ferritin iron core (0.27 nm, consistent with ferrihydrite in the (0–10) orientation). Single Fe atoms are resolved in the liquid environment in (e) near the edge of a GLC. A line profile across the upper left atom is shown as an inset of (e), with each pixel corresponding to 0.99 Å. Reproduced from Ref. 3 with permission from John Wiley and Sons, Inc.

19.3.2 GLC as a Tool to Study Nano-Bio Conjugated Materials: Gold Dimers Conjugated by dsDNA

The motion and structure of double strand DNA (dsDNA) conjugated with Au nanocrystals has been studied in the GLC (Figure 19.8a) [2]. This DNA-assembled nanoconjugate integrates a biological molecule, the linker dsDNA, with inorganic material, two Au nanoparticles, which facilitates tracking of the structure in liquid due to its high contrast (Chapter 16). The moving Au-dsDNA nanoconjugates in liquid appear as clusters of dark circular shapes (Figure 19.8b). In particular, the dynamics of dimers, i.e. pairs of Au nanoparticles tethered by a single piece of dsDNA, can be distinguished from single Au particles, as well as from trimers, which are three Au nanoparticles connected in a linear configuration by two dsDNA bridges (discussed in Section 19.3.3 below). Measurement of the motion of a dimer allows one to infer the configuration and status of its DNA molecule under the electron beam.

A high electron dose is used continuously while imaging dimer motions. Reliable dynamics is observed for up to a few minutes, but then the initially conjugated Au

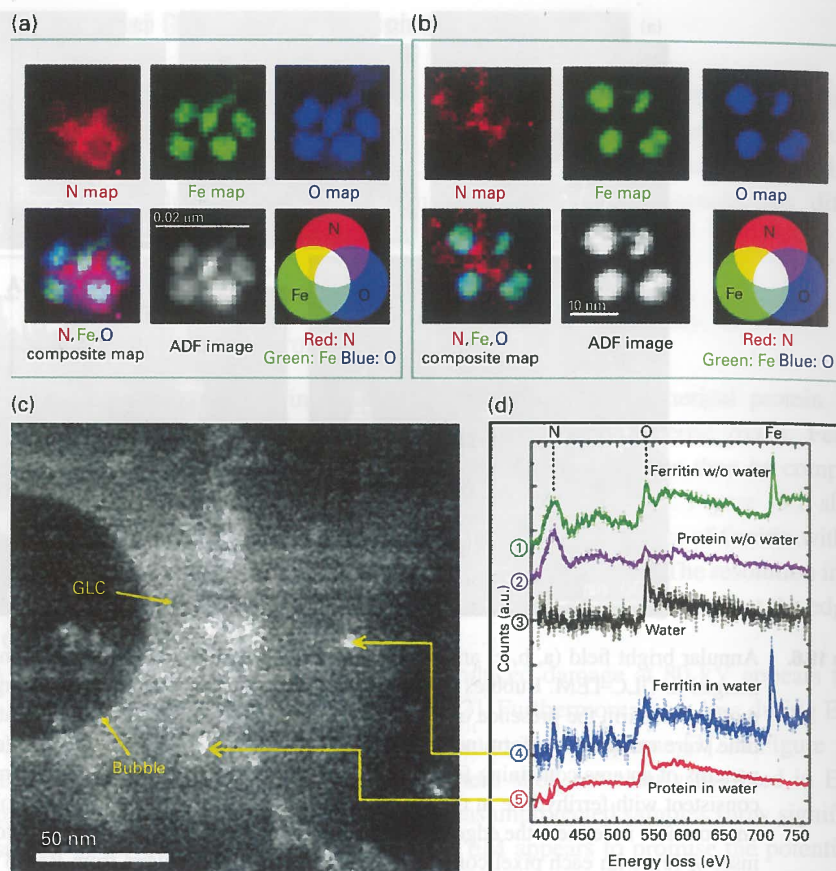


Figure 19.7. To demonstrate stable spectroscopic analysis of biological samples in a graphene sandwich, EELS maps with 1 nm resolution are shown for ferritin molecules (a) sandwiched between graphene sheets and (b) on monolayer graphene. The raw data are filtered using multivariate statistical analysis. The ferritin protein shell is clearly resolved in both cases and the Fe valence is identified as Fe^{3+} distributed across the whole core. But ferritin on graphene shows significantly reduced intensity for oxygen, presumably from sample degradation during imaging. (d) HAADF STEM image of a GLC containing ferritin. (d) EELS spectra of ferritin core, protein shell, or water, from the regions indicated in (c). Reproduced from Ref. 3 with permission from John Wiley and Sons, Inc.

particles are separated or the motion slows down. We assume that prolonged irradiation damages the molecular structure of dsDNA. The integrity of the graphene windows and encapsulated buffer solution can also be compromised after a prolonged time under strong irradiation. As was discussed in Section 19.3.1, control over the dose rate and pixel dwell time is important in order to observe dynamics for a long time without damaging the sample integrity too greatly.

With some understanding of the effect of the beam on the sample, we can compare the motion of various types of Au-dsDNA dimers in the same liquid

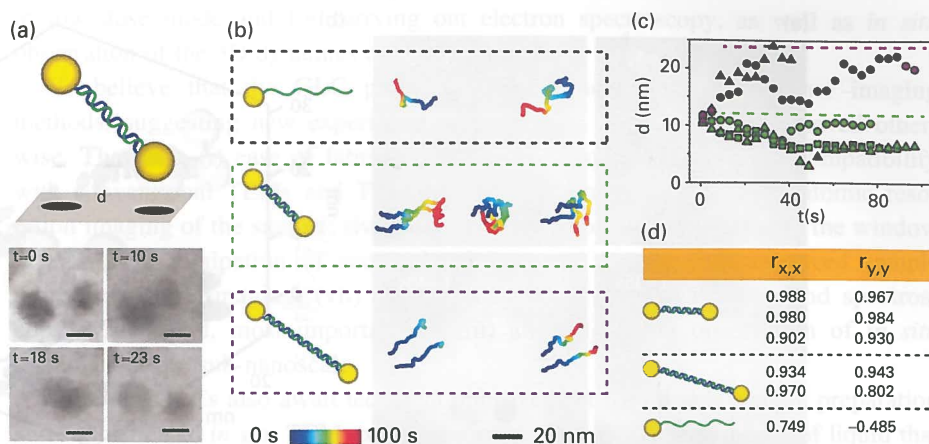


Figure 19.8. Gold nanoparticle dimers conjugated with double strand DNA. (a) Schematic of a dimer and its 2D projection, and representative TEM images of a rotating dimer showing different orientations. Scale bar 5 nm. (b) Various Au nanocrystal trajectories color coded with time in the same liquid pocket: individual particles (top, black box), dimers linked by 42 base pair dsDNA (middle, green box), and dimers linked by 84 base pair dsDNA (lower, purple box). (c) The fluctuation of projected interparticle distance with time for three 42 base pair Au dimers (green data points) and two 84 base pair Au dimers (purple data points). The dotted lines indicate the maxima of interparticle distances. (d) Measured Pearson's correlation coefficients showing the degree of linear correlation of x ($r_{x,x}$) and y ($r_{y,y}$) components of two trajectories. Au dimers conjugated by dsDNA strands show correlated motion for a prolonged time during imaging. Reproduced from Ref. 2 with permission from the American Chemical Society.

pocket. Figure 19.8c shows 2D projected trajectories for Au-single strand DNA, short Au-dsDNA-Au (42 base pair DNA), and long Au-dsDNA-Au (84 base pair DNA) encapsulated in one liquid pocket. Several aspects of the clustered trajectories of Au-dsDNA dimers confirm that the structural integrity of the dsDNA linkers is intact, holding adjacent nanocrystals over a prolonged period of imaging. The projected interparticle distance for each Au nanocrystal pair fluctuates but has a maximum that depends on the length of the dsDNA bridges (Figure 19.8c), while the trajectories of the paired particles show a high positive Pearson's correlation coefficient, with free particles showing low or even negative correlation (Figure 19.8d).

19.3.3 Real-Time Observation of 3D Configuration and Motions: dsDNA Conjugated Gold Nanoparticle Trimers

These types of experiments can be extended to more complex structures to provide an opportunity to track motion and configuration change in 3D [2]. For trimers, an iterative optimization method of frame-based capture of the continuous motion can be applied to extract both the rotational and translational motions (color-coded arrows and color-coded dots in Figure 19.9b, respectively) without *a priori*

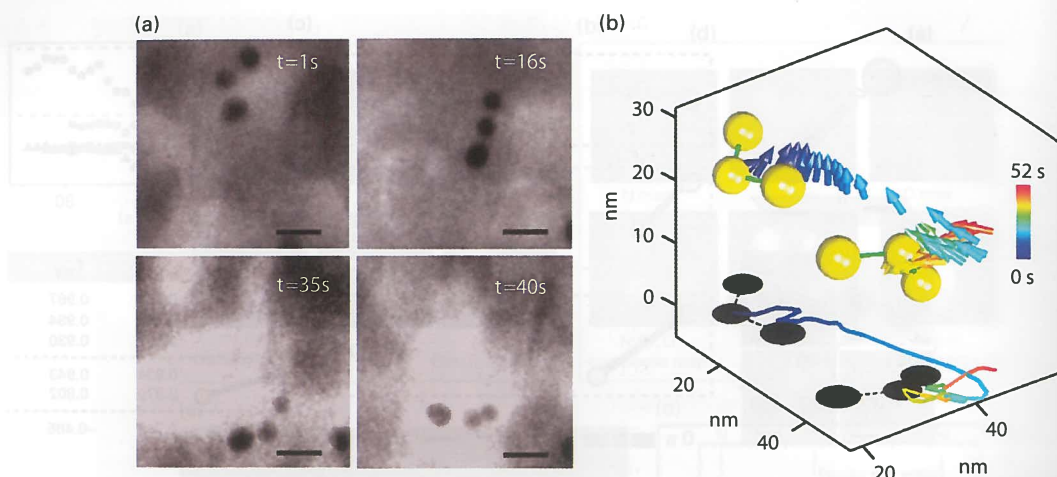


Figure 19.9. Three-dimensional configuration and motion of a Au trimer multiply conjugated with dsDNA. (a) Series of images of a trimer. The scale bar is 10 nm. (b) The reconstructed motion of the trimer in 3D: rotational (color-coded arrows) and translational (color-coded dots for the central nanocrystal). The two trimer diagrams (yellow spheres linked by green lines) show the configuration at $t = 1\text{ s}$ and 40 s , respectively. Reproduced from Ref. 2 with permission from the American Chemical Society.

knowledge of the structural details of the trimers. The iteration method works by using the 2D projected interparticle distances of the two bridges of the trimer and their ratio to reconstruct the 3D orientation of the trimer in each frame. Repeating the same process for all frames, the standard deviation of the interparticle distances of the three Au particles calculated from the extracted 3D coordinates in each frame is used as a reference to fine tune the original structure of the trimer. Mathematical details of this method have been published elsewhere [2]. The principles of reconstructing 3D structure and motion from 2D projections can readily be extended to other structures in order to relate their 3D configuration and motion in solution to their function.

19.4 Future Directions

In this chapter we have summarized the recent developments in graphene liquid cell TEM and the use of the GLC in studying liquid sample dynamics at high resolution. The GLC has enabled the study of colloidal nanocrystal growth and diffusion processes with unprecedented resolution and without significant perturbation by substrate interactions. The GLC has also shown its worth as a platform for studying general protein samples

in low dose mode and for carrying out electron spectroscopy, as well as *in situ* observation of the 3D dynamics of nanocrystal-DNA nanoconjugates.

We believe that the GLC provides multiple advantages over other imaging methods, suggesting new experimental capabilities that cannot be achieved otherwise. These are (i) ease of fabricating a liquid sample for TEM; (ii) compatibility with conventional TEMs and TEM holders; (iii) the opportunity for atomic resolution imaging of the sample; (iv) the chemical and physical inertness of the window material; (v) dissipation of accumulated heat and charge; (vi) enhanced sample protection while imaging; (vii) compatibility with versatile imaging and spectroscopy modes; and, most importantly, (viii) allowing direct observation of *in situ* dynamics at the sub-nanoscale.

However, GLCs also await technical improvement for reliable sample preparation and sophisticated *in situ* TEM experimentation. First of all, the amount of liquid that is encapsulated is not well controlled, especially in first generation GLCs. The efforts put into development of second and third generation GLCs will hopefully lead to more reliable *in situ* experiments. Fabricating functional components within the liquid enclosure, such as electrodes or heaters, can also be possible in principle, expanding the uses of GLC in high resolution TEM studies of reactive liquid environments.

A wide range of dynamics, interactions, and reactions await direct *in situ* GLC-TEM observation in materials sciences, physical chemistry, and biochemistry, correlating structure and development with reactions and functions in a realistic environment. The GLC-TEM satisfies requirements that might otherwise be considered incompatible. It provides high resolution imaging capability while maintaining a realistic liquid condition free from interactions with the windows. For X-ray analysis and EELS measurements, it minimizes unnecessary scattering and the strong core-loss signal usually associated with the presence of Si and N in non-graphene liquid cells. These requirements are not easily satisfied with other existing imaging tools, so we expect that the GLC will be applied to diverse dynamics that either have not been explored or need more detailed understanding. The few topics introduced above are the first steps in applying GLC-TEM for studying colloidal nanoparticle growth, diffusion dynamics at the nanoscale, hydrated biological specimens, and nano-bio interfaced materials. Following these initial studies, the next generation GLC devices we have introduced here will readily be applied to study diverse fluid samples as they evolve and function in time. Self-assembly at different length scales of atoms, nanocrystals, proteins, and macromolecules can benefit from GLC-TEM. Protein-to-protein interactions and macromolecule/polymer dynamics are examples where GLC-TEM will enable observation of delicate systems. Low dose imaging of protein molecules has already demonstrated the capacity of GLC TEM in studying such samples. The recent developments in direct electron detectors are expected to further improve imaging conditions by enhancing signal-to-noise ratio for even lower electron doses, suggesting promising directions for future research.

References

1. J. M. Yuk, J. Park, P. Ercius *et al.*, High-resolution EM of colloidal nanocrystal growth using graphene liquid cells. *Science*, **336** (2012), 61–64.
2. Q. Chen, J. M. Smith, J. Park *et al.*, 3D motion of DNA-Au nanoconjugates in graphene liquid cell electron microscopy. *Nano Lett.*, **13** (2013), 4556–4561.
3. C. Wang, Q. Qiao, T. Shokuhfar and R. F. Klie, High-resolution electron microscopy and spectroscopy of ferritin in biocompatible graphene liquid cells and graphene sandwiches. *Adv. Mater.*, **26** (2014), 3410–3414.
4. A. De Clercq, W. Dachraoui, O. Margeat *et al.*, Growth of Pt–Pd nanoparticles studied in situ by HRTEM in a liquid cell. *J. Phys. Chem. Lett.*, **5** (2014), 2126–2130.
5. N. Mohanty, M. Fahrenholtz, A. Nagaraja, D. Boyle and V. Berry, Impermeable graphenic encasement of bacteria. *Nano Lett.*, **11** (2011), 1270–1275.
6. P. Ercius, K. Kim, A. Zettl *et al.*, In-situ observations of Pt nanoparticle growth at atomic resolution using graphene liquid cells and Cc correction. *Microsc. Microanal.*, **18** (2012), 1096–1097.
7. R. R. Nair, P. Blake, J. R. Blake *et al.*, Graphene as a transparent conductive support for studying biological molecules by transmission electron microscopy. *Appl. Phys. Lett.*, **97** (2010), 153102.
8. Z. Lee, K. Jeon, A. Dato and R. Erni, Direct imaging of soft–hard interfaces enabled by graphene. *Nano Lett.*, **9** (2009), 3365–3369.
9. W. Regan, N. Alem, B. Alemán *et al.*, A direct transfer of layer-area graphene. *Appl. Phys. Lett.*, **96** (2010), 113102.
10. J. E. Evans, K. L. Jungjohann, N. D. Browning and I. Arslan, Controlled growth of nanoparticles from solution with in situ liquid transmission electron microscopy. *Nano Lett.*, **11** (2011), 2809–2813.
11. H. Zheng, S. A. Claridge, A. M. Minor, A. P. Alivisatos, and U. Dahmen, Nanocrystal diffusion in a liquid thin film observed by in situ transmission electron microscopy. *Nano Lett.*, **9** (2009), 2460–2465.
12. T. J. Woehl, J. E. Evans, I. Arslan, W. D. Ristenpart and N. D. Browning, Direct in situ determination of the mechanisms controlling nanoparticle nucleation and growth. *ACS Nano*, **6** (2012), 8599–8610.
13. U. M. Mirsaidov, H. Zheng, Y. Casana and P. Matsudaira, Imaging protein structure in water at 2.7 nm resolution by transmission electron microscopy. *Biophys. J.*, **102** (2012), L15–L17.
14. H. Zheng, U. M. Mirsaidov, L.-W. Wang and P. Matsudaira, Electron beam manipulation of nanoparticles. *Nano Lett.*, **12** (2012), 5644–5648.
15. M. T. Proetto, A. M. Rush, M.-P. Chien *et al.*, Dynamics of soft nanomaterials captured by transmission electron microscopy in liquid water. *J. Am. Chem. Soc.*, **136** (2014), 1162–1165.
16. K. L. Jungjohann, S. Bliznakov, P. W. Sutter, E. A. Stach and E. A. Sutter, In situ liquid cell electron microscopy of the solution growth of Au–Pd core-shell nanostructures. *Nano Lett.*, **13** (2013), 2964–2970.
17. U. M. Mirsaidov, H. Zheng, D. Bhattacharya, Y. Casana and P. Matsudaira, Direct observation of stick-slip movements of water nanodroplets induced by an electron beam. *Proc. Natl. Acad. Sci. USA*, **109** (2012), 7187–7190.
18. L. R. Parent, D. B. Robinson, P. J. Cappillino *et al.*, In situ observation of directed nanoparticle aggregation during the synthesis of ordered nanoporous metal in soft templates. *Chem. Mater.*, **26** (2014), 1426–1433.

19. H. Zheng, R. K. Smith, Y.-W. Jun *et al.*, Observation of single colloidal platinum nanocrystal growth trajectories. *Science*, **324** (2009), 1309–1312.
20. H.-G. Liao, L. Cui, S. Whitlam and H. Zheng, Real-time imaging of Pt₃Fe nanorod growth in solution. *Science*, **336** (2012), 1011–1014.
21. J. Park, H. Zheng, W. C. Lee *et al.*, Direct observation of nanoparticle superlattice formation by using liquid cell transmission electron microscopy. *ACS Nano*, **6** (2012), 2078–2085.
22. J. M. Grogan, N. M. Schneider, F. M. Ross and H. H. Bau, Bubble and pattern formation in liquid induced by an electron beam. *Nano Lett.*, **14** (2014), 359–364.
23. N. M. Schneider, M. M. Norton, B. J. Mendel *et al.*, Electron–water interactions and implications for liquid cell electron microscopy. *J. Phys. Chem. C*, **118** (2014), 22373–22382.
24. V. P. Adiga, G. D. Dunn, A. P. Alivisatos and A. Zettl, Liquid flow cells having graphene on nitride for microscopy. US Patent Application No. US 20160042912 A1.
25. M. E. Holtz, Y. Yu, J. Gao, H. D. Abruña and D. A. Muller, In situ electron energy-loss spectroscopy in liquids. *Microsc. Microanal.*, **19** (2013), 1027–1035.
26. J. Polte, R. Erler and A. F. Thu *et al.*, Nucleation and growth of gold nanoparticles studied via in situ small angle X-ray scattering at millisecond time resolution. *ACS Nano*, **4** (2010), 1076–1082.
27. M. Harada and E. Katagiri, Mechanism of silver particle formation during photoreduction using in situ time-resolved SAXS analysis. *Langmuir*, **26** (2010), 17896–17905.
28. J. Polte, T. T. Ahner, F. Delissen *et al.*, Mechanism of gold nanoparticle formation in the classical citrate synthesis method derived from coupled in situ XANES and SAXS evaluation. *J. Am. Chem. Soc.*, **132** (2010), 1296–1301.
29. X. Lu, M. Rycenga, S. E. Skrabalak, B. Wiley and Y. Xia, Chemical synthesis of novel plasmonic nanoparticles. *Annu. Rev. Phys. Chem.*, **60** (2009), 167–192.
30. P. Schapotschnikow, R. Pool and T. J. H. Vlugt, Molecular simulations of interacting nanocrystals. *Nano Lett.*, **8** (2008), 2930–2934.